Opto-Acoustic Interactions in Gravitational Wave Detectors: Comparing Flat-Top Beams with Gaussian Beams

S. Gras,* D.G. Blair, and L. Ju

School of Physics, The University of Western Australia,

35 Stirling Highway, Crawley, WA 6009, Australia.

(Dated: March 18, 2009)

Abstract

To reduce the thermal noise in the next generation of gravitational wave detectors, flat-top beams have been proposed to replace conventional Gaussian beams, so as to obtain better averaging over the Brownian motion of the test masses. Here we present a detailed investigation of the unwanted opto-acoustic interactions in such interferometers, which can lead to the phenomenon of parametric instability. Our results show that the increased overlap of the Mesa beams with the test masses leads to approximately 3 times as many unstable modes in comparison to a similar interferometer with Gaussian beams.

PACS numbers:

*Electronic address: sgras@cyllene.uwa.edu.au

I. INTRODUCTION

Future gravitational wave (GW) astronomy requires detection of astronomical sources at a significant rate, with a signal-to-noise ratio well above unity. The sensitivity of the present detectors [1–3] is still far from this goal. Advanced LIGO is expected to be the first detector in the required sensitivity regime. However, further advances are required. An intensive effort is underway to define techniques which will enable improved sensitivity.

To achieve improved sensitivity beyond Advanced LIGO, two major noise sources must be reduced: thermal surface vibration of the test masses (thermal noise) and photon counting in the dark port of the interferometer (shot noise).

There have been three alternative suggestions for the minimisation of thermal noise. One is the choice of the material for the test masses. Such materal should be chracterised by low acoustic and thermo-elastic losses [4]. The second is the use of cryogenics to directly reduce the amplitude of thermal fluctuations [5, 6]. The third is to minimise the mirror thermal noise by improving the averaging of surface vibration. This can be achieved by increasing the area of the optical beam that interacts with the test mass surface. Ideally, a beam with a flat wavefront would be the best option since the surface sampling would be the most effective. However, such a beam profile would not sustain resonance in a cavity with finite mirrors. A practical compromise is to use a beam with a fairly flat intensity profile covering most of the mirror surface, dropping steeply in intensity towards the edges so as to ensure low diffraction losses [7, 8]. There have been several proposals for a different beam geometry in interferometers. The first was the flat-top or Mesa beam [9, 10]. Since then, others have proposed the use of high-order Laguerre-Gaussian modes [11, 12], and Conical beams [13]. Mesa beams have been successfully created in optical resonators [14]. Numerical studies have shown that this type of flat-top beam can reduce mirror thermal noise by a factor of ~ 3 with respect to conventional Gaussian beams [15, 16]. Moreover, if flat-top beams are used in an Advanced LIGO type interferometer, the entire sensitivity curve can be limited by quantum noise.

The next generation of GW detectors requires the use of high optical power to reduce the contribution of photon shot noise. For example, in Advanced LIGO approximately 800 kW of optical power will circulate in the arm cavity. Unfortunately, high optical energy density in the interferometer arms can also be responsible for a non-linear interaction of the electro-

magnetic field with the mirror substrate acoustic motion. On one hand, high optical power improves photon counting and thus lowers the shot noise, but on the other hand, high power can also increase the chance of the carrier being scattered into a higher order mode via an opto-acoustic interaction.

The scattering of light by acoustic waves is a well-known phenomenon. There are three major mechanisms responsible for scattering in optical cavities: the elasto-optical mechanism, the length modulation mechanism, and the ripple mechanism. In the elasto-optical mechanism, the refractive index variation induced by an acoustic wave acts as a grating in the medium through which light propagates, and causes scattering. If this process occurs in an optical cavity, the scattered light can stimulate acoustic wave excitation in the medium [17, 18]. Such scattering with positive feedback is called stimulated Brillouin scattering (SBS). For SBS, the modulation frequency is $\sim 10^{10}$ Hz. In the length modulation mechanism, a rigid mirror attached to an acoustic resonator creates a frequency modulation. There is no change in the spatial structure of the scattered mode [19]. Usually, the optical sidebands which are created occur within the cavity linewidth. In terms of spatial structure, only two modes participate in the scattering process: one optical and one acoustic mode - this is therefore a 2-mode process. This 2-mode interaction has been widely adopted in mode cooling [20], optical springs experiments [21], and in creating linear motion transducers [22].

The topic of this paper involves the ripple mechanism. It is an opto-acoustic interaction which combines both SBS and intercavity modulation. The optical cavity length is not modulated by the translation motion of the mirror, but by the ripple-like standing waves on the surface associated with the bulk internal motion of the mirror substrate due to its acoustic modes. The surface vibration of the mirror in the optical cavity scatters a carrier mode into a transverse optical mode (TEM) of the cavity. This TEM can excite and amplify an acoustic mode by the same feedback mechanism as in SBS. Such a scattering process is characterised by a simultaneous triple resonance of a carrier optical mode, a transverse optical mode, and an acoustic mode. We call this process a 3-mode interaction.

Zhao et al. [23] have experimentally shown using an 80 m cavity that the interaction of photons with test mass surface vibration indeed occurs. This was the first evidence that cavities may sustain such 3-mode interactions. Numerous previous experiments have reported 2-mode interactions [24].

For various reasons discussed further below, 3-mode interactions are macroscopic, involving

acoustic modes of the mirror in the frequency range $10^4 - 10^6$ Hz, and transverse modes up to 8th order. We normally refer to the transverse modes as high order modes (HOMs); these HOMs lie above or below the main cavity frequency.

Two opposite processes are allowed in opto-acoustic scattering. The first, corresponding to acoustic amplification, which occurs when $\omega_0 - \omega_{hom} \simeq \omega_m$. The second, corresponding to acoustic dampingand occurs when $\omega_{hom} - \omega_0 \simeq \omega_m$. Such 3-mode interactions depend on the frequency match between the carrier mode ω_0, the higher-order mode ω_{hom}, and the acoustic mode ω_m, as well as on there being a spatial overlap of the acoustic mode shape and the transverse optical mode (see Fig. 1). If the interaction strength is large enough, then the acoustic mode amplitude can experience exponential growth over a short time ranging from tens of milliseconds up to minutes (e.g. see [25]). This phenomenon is called parametric instability (PI).

Parametric instability was first analysed by Braginsky et al. [26], Kells et al. [27], and Zhao et al. [28] for the case of a single optical cavity. Braginsky et al. showed that PI is a potentially serious problem for the next generation of GW detectors. Kells et al. pointed out that by ignoring damping processes, the PI models can overestimate the number of unstable modes. In detailed analysis of a more realistic case, Zhao et al. showed that PI was likely in Advanced LIGO. Similar results were obtained by Bantilan et al. [29]. Both analyses showed that PI can occur for acoustic modes lying in the range from $\sim$ 10 kHz up to $\sim$ 100 kHz for the Advanced LIGO type interferometer. Since then, the analysis has been refined to consider the effect of power and signal recycling cavities [30–34].

The results of this modelling show that mismatch between cavities significantly affects PI; both power recycling and signal recycling can significantly change the instability conditions. However, the potential for instability is well estimated by considering a single cavity. More complex interferometer configurations can show both increased and reduced levels of instability, depending on precisely defined but poorly designed details, such as errors in the radii of curvature of the mirrors. For comparing two types of optical cavity, it is sufficient to consider a single optical cavity.

PI can be described by a parametric gain parameter R. If R $>$ 1, then an acoustic mode becomes unstable. For the case of the single optical cavity, the parametric gain of an acoustic

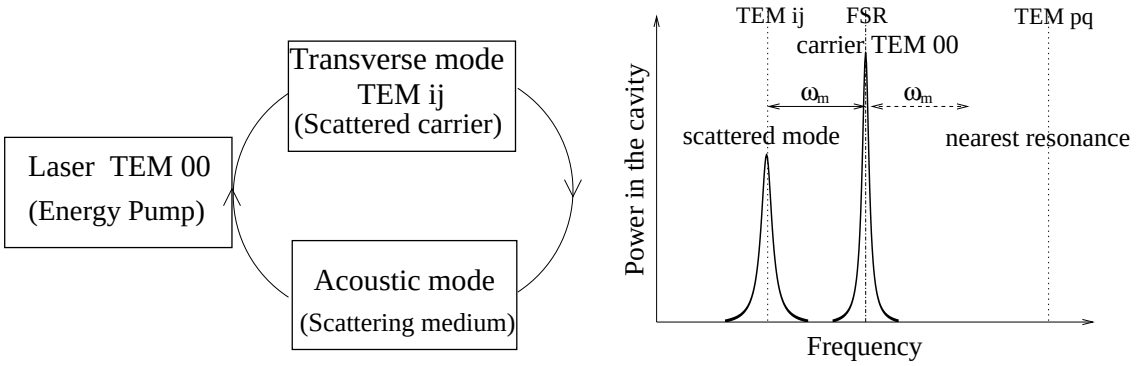

FIG. 1: The idea of 3-mode interactions. The left plot represents the scheme by which three modes interact with each other. The carrier mode is pumped into cavity where it experience scattering on the mirror surface profiled by a particular acoustic modes. If the mirror surface motion spatially overlaps with the electric field distribution of a transverse optical mode, there is a possibility for the carrier mode to be scattered into this mode. The right frequency combination of all three modes can result in amplification of acoustic modes via the transverse optical mode, as represented in the diagram by a closed loop. The frequency structure is shown on the right graph. The asymmetry of the modal structure of optical cavities means that only one sideband participate in the interaction. This could be either red or blue-shifted. The graph shows an example of the excitation process due to a red-shifted sideband. Note that in practise there is no special requirement for the pump energy to be in the form of the TEM 00 mode: this is just the conventional choice for the pump mode.

mode is:

$$R = \frac{4PQ_mQ\Lambda}{mcL\omega_m^2}\left(\left(1+\Delta\omega_s^2/\delta_s^2\right)^{-1} - \left(1+\Delta\omega_a^2/\delta_a^2\right)^{-1}\right), \tag{1}$$

where $\Delta\omega_{s/a} \equiv \omega_{0/hom} - \omega_{hom/0} - \omega_m$ is the resonance condition describing either excitation or damping of the acoustic modes, δ is the half linewidth of the optical mode, m is the mass of the test mass, and L is the length of the cavity. According to the above formula, parametric instability is directly proportional to the circulating power P in the cavity, the acoustic mode quality factor Q_m, the optical mode quality factor Q, and the overlapping parameter Λ. A detailed description of Λ is given in Sec. IV.

To properly estimate R values, both acoustic and optical mode structures must be known. Frequencies and spatial distributions of modes are necessary to determine resonance condi-

tions and overlapping parameters, respectively. Since the cavity losses determine the optical quality factor, a careful analysis of optical losses must also be taken into account.

Ju et al. [35] showed that multiple interactions can occur simultaneously, further increasing the problem of PI. The parametric gain for any acoustic mode results from a superposition of multiple interactions with high-order optical modes (HOMs). Each HOM, depending on its frequency, can contribute to either excitation or damping of the internal vibrations of the test masses. For the purpose of this paper, we adopted a decomposition method. Based on the multi-mode nature of this phenomenon, the effective parametric gain of any acoustic mode can be written as:

$$R = \frac{4PQ_m}{mcL\omega_m^2}\left(\sum^{HOMs} r_s - \sum^{HOMs} r_a\right). \tag{2}$$

However, the mode superposition method can be problematic. The exact evaluation of the scattered beam requires complete basis set of the cavity modes. Moreover, some basis elements represented by highly diffractive HOMs (low finesse modes) can substantially differ from their analytical counterparts. Therefore an analytically estimated basis can be incorrect [36]. For this reason, a numerical approach seems to be the most suitable in order to calculate highly lossy HOMs for the total scattered field representation. Ideally, the summation in Eqn. 2 should be carried out over an infinite number of modes. However, due to the increase of diffraction losses with optical mode order, combined with a reduced magnitude of the overlapping parameter at large frequency differences, it is generally a good approximation to terminate the summation at the 8th order of the optical mode. The geometry mismatch (corresponding to a small overlapping parameter) is the dominant factor which determines the summation threshold. Thus relatively low-loss HOMs above 8th order make insignificant contributions to the parametric gain for the beam geometries considered here.

Parallel to the development of the superposition method, Kells [37] developed another way to estimate parametric gain. Instead of the multi-mode analysis, Kells treated the scattered net field as a whole, avoiding individual modes. The analysis of an Advanced LIGO single cavity done by Bantilan and Kells [29] confirmed that these two methods are equivalent to each other.

Note that the gain contributions (Eqn. 2) of the Stokes processes r_s and the anti-Stokes processes r_a differ in sign, while their magnitudes are given by $r_{s/a} \equiv Q\Lambda(1 + \Delta\omega_{s/a}^2/\delta_s^2)^{-1}$

(see Eqn. 1). Thus, the effective gain can be either positive or negative, depending on whether the excitation or damping process is dominant in a multiple HOM system. A negative value of R indicates that the acoustic mode is damped, a positive value indicates that damping is reduced, and R > 1 indicates parametric instability.

The analysis for Gaussian beams has shown the strong sensitivity of the system to very small changes in cavity parameters, which strongly affect the resonance condition. This sensitivity is such that mirror imperfections are likely to dominate actual observations. As has been previously emphasised, this means that results must be interpreted as being a statistical prediction of the probability of the instability, rather than a precise prediction of actual behaviour.

In view of the above, for this paper we have restricted our analysis to a single cavity. The prediction of the instability was determined by the generalisation of Eqn. 2. Test masses were assumed to be made of sapphire. There are three reasons for this. Firstly, as discussed by Ju et al. [38], the high velocity of sound in sapphire means that the acoustic mode density is lower. This has the advantage, in general, of reducing the possibility of opto-acoustic interactions, and thereby of decreasing the expected number of unstable acoustic modes. Secondly, the smaller number of acoustic modes also means that the computational task is easier, reducing the very long CPU times required for numerical analysis. Thirdly, sapphire is the proposed material for the LCGT detector in Japan, and it is a candidate for third generation cryogenic detectors for which Mesa beams might be considered.

The motivation of this work is to compare interferometers with flat-top beams to those using conventional Gaussian beams. Comparison of all the other beams, mentioned earlier, is beyond the scope of this paper. Each will have a different pattern of opto-acoustic interactions, determined mainly by an opto-acoustic overlap integral, and by the spectrum of higher-order modes.

We consider three different cavity types: Gaussian near-concentric (CG), Mesa near-flat (FM), and Mesa near-concentric (CM). Due to the high susceptibility of the near-flat FM cavity to radiation pressure induced tilt instability [39], we only focus on concentric cavities. However, the FM case is useful for estimating and validating CM cavity parameters.

For definitiveness, we have chosen parameters similar to those used to define Advanced

LIGO. Our purpose is to obtain an estimate of the relative differences between the Mesa and Gaussian beam cavities. These relative differences are not strongly dependent on the detailed parameter choice.

Analysis of PI requires detailed modelling of both acoustic and optical modes. In Sec. II, we describe the modal analysis of the acoustic modes. In Sec. III we describe the methods used to determine the optical structure of the Gaussian and Mesa beam cavities: resonances, mode shapes, and losses associated with cavity structure. In Sec. IV, we describe the estimation of the overlapping parameter Λ for the optical and acoustic modes, which determines the possible amplitude of opto-acoustic interactions. Finally, in Sec. V we present the results for the PI analysis of the two systems.

II. TEST MASS ACOUSTIC MODE MODELLING

To determine the mode shapes u and frequencies ω_m of test mass acoustic modes, we used Finite Element Analysis (FEA). Sapphire anisotropy and the detailed geometry preclude analytical solutions.

In FEA, mathematical operations are performed on nodes which are grouped into elements. The displacement vector u in each node can be written as:

$$M_{ab}\frac{\partial^2 u_i^b}{\partial t^2} + K_{aibk}u_k^b = 0, \tag{3}$$

where M_{ab} is the element of the global mass matrix, and K_{aibk} is the element of the global stiffness matrix, defined as follows:

$$K_{aibk} = \int_s C_{ijkl}\frac{\partial\varphi^a\left(\vec{\xi}\right)}{\partial\xi_j}\frac{\partial\varphi^b\left(\vec{\xi}\right)}{\partial\xi_l}dV, \tag{4}$$

$$M_{ab} = \int_s \rho\varphi^a\left(\vec{\xi}\right)\varphi^b\left(\vec{\xi}\right)dV. \tag{5}$$

C is the 4-rank compliance tensor (see Table I), ρ is the density of the test mass, and $\varphi(\vec{\xi})$ is the position-dependent shape function, defined as $u_i\left(\vec{\xi}\right) = \varphi^q\left(\vec{\xi}\right)u_i^q$. This shape function is an interpolation which specifies the vector u at an arbitrary position on the test mass. Since the shape function refers only to a single element, the K and M matrices are constructed by rearranging and adding element stiffness and mass matrices, respectively. Substituting

TABLE I: Notation and values for the main parameters used in this paper.

Quantity	Value	Description
Test mass:		
r_t	0.16 m	Radius
d_t	0.2 m	Thickness
ϕ_t	0.5 deg	Back face wedge angle
C	C_{11}=498.1 C_{12}=C_{13}=110.9	Non-zero elements of the compliance
	C_{22}=C_{33}=496.8 C_{23}=163.6	matrix [GPa] for m-axis sapphire crystal[a]
	C_{35}=-C_{25}=-C_{46}=23.5	
	C_{44}=166.6 C_{55}=C_{66}=147.4	
ρ	3983 kg/m^3	Density
m	40 kg	Mass of the test mass
Q_m	$1{\cdot}10^7$	Acoustic mode quality factor
Optics:		
L	4000 m	Cavity length
T_{ITM}	1.4 %	Input test mass transmissivity
T_{ETM}	5.0 ppm	End test mass transmissivity
FSR	37.474 kHz	Free spectral range
λ	$1.064{\cdot}10^{-6}$ m	Wavelength
k	$5.9905{\cdot}10^6$ rad/m	Wave number
D	$1.041{\cdot}10^{-1}$ m	Mesa beam radius
R	2050.6 m	Radius of curvature
		for concentric Gaussian mirrors
P	830 kW	Circulating power in the arm cavities

[a]compliance tensor for m-axis is shown in matrix form [40].

$u = \mu_m cos(\omega_m t)$ in Eqn. 3, where μ_m is the eigenvector representing the mode shape of the mth natural frequency ω_i, we can obtain an eigenequation as follows:

$$|K - \omega_i^2 M| = 0. \tag{6}$$

By solving Eqn. 6, we can obtain mode shapes μ_m and mode frequencies ω_m.

Procedures, such as meshing of the model, evaluation of the stiffness, and mass matrices were performed using ANSYS FEA software [41]. To solve Eqn. 6, we chose the Bloc-Lanczos method [42], which is one of the standard ANSYS approaches for a model with a large number of nodes.

To ensure that all acoustic modes had correct shapes, and were not affected by poor meshing, we created a test mass model with $\sim$ 140000 nodes. The model was meshed with 8-noded linear 3D elements. The test mass was assumed to be a cylinder with 45^o chamfers on the corners, and with a back face tilted 0.5^o with respect to the front face (for separation of surface reflections). The dimensions of this 3D model are shown in Table I. The substrate was chosen to be a sapphire crystal with the m-axis parallel to the circumference of the cylinder.

The eigenvectors μ_m obtained from the solution were normalised to unity such that the largest component was 1. We calculated the first 800 acoustic modes. The resonant frequencies of the model are shown in Fig. 2. It is useful to scale them relative to the free spectral range (FSR) of the optical cavity. For an opto-acoustic interaction, this mode frequency must coincide with an optical mode frequency difference ($\Delta = |\omega_{hom} - \omega_{00}|$). Almost all of the 800 modes sit within the 0-3 FSR range.

It is clear that the acoustic mode density increases with mode frequency. The mean mode spacing reduces to $\sim$ 50 Hz at the high end of the range. Thus, there is a larger probability for higher-frequency acoustic modes to be in resonance with optical modes.

Each acoustic mode frequency and mode shape, determined in the above analysis, is stored in a database for the purpose of estimating PI once the optical modes have been determined.

III. OPTICAL MODE STRUCTURE

In the opto-acoustic scattering, the strength of the scattering interaction is governed by resonance conditions defined by $\Delta\omega$ having a low value and Λ having a high value. Therefore,

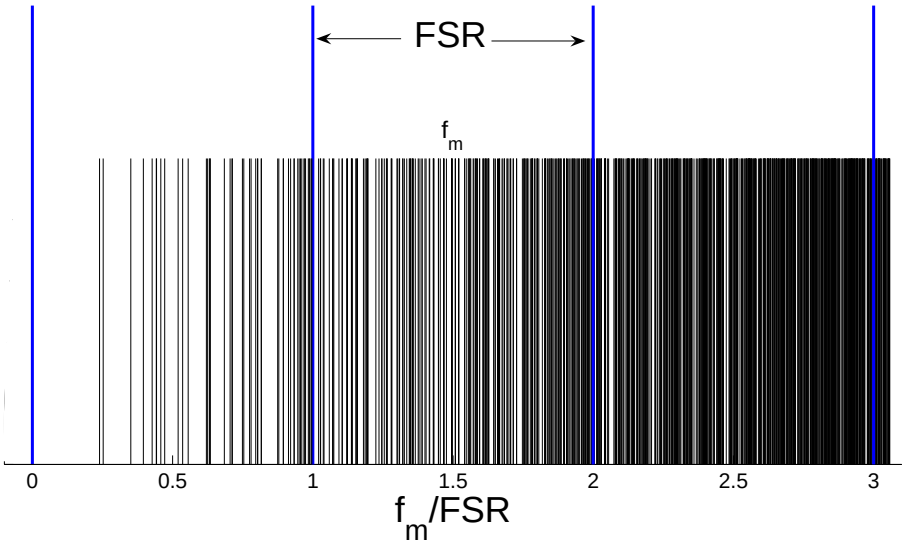

FIG. 2: Acoustic modes of the sapphire test mass model. Mode frequencies f_m are represented in terms of the Free Spectral Range (FSR) of the optical cavity. The 800 modes plotted here cover the frequency range up to the 3rd FSR. This covers all the modes that can potentially contribute to parametric instability.

besides determining the acoustic modes, it is necessary to find the frequencies and shapes of the higher-order optical modes.

An analytical solution of the beam propagating in the cavity is well established for Gaussian beams. However there is no simple analytic solution for flat-top beams. In addition, the analytic solution for a Gaussian cavity does not accurately represent a real cavity with finite mirrors (see, for example, Barriga et al. [43]). Therefore, a numerical analysis again becomes essential to find the mode shapes and frequencies and for both types of beams.

A. Cavity eigenstates and eigenvalues

The optical cavity mode structure and mode shapes were solved using the cavity eigenvalue equation. For this purpose, we use the Fresnel-Kirchhoff propagation equation describing the electric field $E(\vec{r}, z)$ on mirror 2, propagating from mirror 1 in a two mirror cavity:

$$E_2\left(\vec{r_2}, L\right) = -\frac{ik}{2\pi} \int\int_S G\left(\vec{r_2}, \vec{r_1}\right) E_1\left(\vec{r_1}, 0\right) F\left(\theta\right) d^2\vec{r_1}, \tag{7}$$

where $F(\theta)$ is the obliquity factor: $F(\theta) = 0.5(1 + cos\theta)$. For long baselines $F(\theta) \approx 1$, where $k = \frac{2\pi}{\lambda}$ is the wave number, and G is the propagation kernel, defined as:

$$G\left(\vec{r_2}, \vec{r_1}\right) = \frac{ik}{2\pi\eta} e^{-ik\eta}. \tag{8}$$

Here, η is the distance between any two arbitrary points on the opposite mirror, given by

$$\eta = \sqrt{\varsigma^2 + |\vec{r_2} - \vec{r_1}|^2}, \tag{9}$$

where

$$\varsigma = L - h\left(\vec{r_2}\right) - h\left(\vec{r_1}\right). \tag{10}$$

In the above equations, the vector $\vec{r}$ is the transverse distance from the centre of the mirror, L is the cavity length, and h is the mirror profile height. The mirror profiles h were constructed from the non-normalised electric field distribution of the Mesa and Gaussian beams as seen at the reflecting surface of each mirror in a symmetrical cavity, using Eqns. 11 and 12, respectively, as follows:

$$u_{00}^{MF}\left(D, \vec{r}\right) = \int_{r' \leq D} exp\left[\frac{-k\left(\vec{r} - \vec{r'}\right)^2 (1+i)}{2L}\right] d^2\vec{r'}, \tag{11}$$

$$u_{00}^{GC}\left(R, \vec{r}\right) = exp\left(-i\left[\frac{kL}{2} + \frac{ik|\vec{r}|^2}{2R} - arctan\left(\frac{2R - L}{L}\right)^{1/2}\right]\right). \tag{12}$$

Here, D is the Mesa beam radius, and R is the radius of curvature for the Gaussian beam. We use D here to be consistent with the original work on Mesa beams [9, 10]. The Mesa beam is obtained by superposition of the optimal Gaussian beams, i.e. beams with the best combination of the minimum beam diameter and best collimation over the distance from the cavity waist to the mirror position. Optimal beams ensure that the Mesa beam edge has optimally sharp falloff. The integration in Eqn. 11 is carried out over a circle with radius D, which defines the Mesa beam. We assume the Mesa beam to have a radius of $D = 4\sqrt{L/k}$ = 0.1041 m (4× bigger than the optimal Gaussian beam waist), which corresponded to a Gaussian beam with $R = 2050.6$ m, with the same diffraction losses of 19.5 ppm. We chose such a beam size to allow comparison with previous work on Mesa beams with the same beam radius [39, 44].

Note that we desire each of the beams to be a steady stable-state beam in the cavity. The

stability of the beam is achieved when its profile duplicates itself after a round trip. In other words, the reflected beam seen on mirror 2 is the phase-conjugate replica of the beam on mirror 1 for the symmetric cavity case, $E_2(\vec{r_2}, L) = E_1^*(\vec{r_1}, 0)$. Therefore, to ensure that beam profiles (Eqns. 11 and 12) would remain unchanged at each mirror position as light bounces back and forth, the mirror phase must match with the wavefront of the beam [45]. The relation between mirror shape h and the beam wavefront is $kh(\vec{r}) = u'(\vec{r})$, where $u'(\vec{r})$ is the wavefront of the beam, defined as: $u'(\vec{r}) = Arg(u_{00}(\vec{r}) - u_{00}(0))$. We should emphasise here that due to the finite size of the mirrors (see Table I), diffraction leads to a change in the profile of the beam which in turn can cause a deviation of the numerically obtained beam profile from that of the input analytical beam. However, this effect is negligible for low loss beams. As we show later, both the Gaussian and Mesa beam profiles have small diffraction losses. Also, comparison of these mode shapes with numerically obtained beams from constructed cavities, give similar results within numerical error.

There are two possible mirror shapes for which a resonating carrier mode would have exactly the same intensity profile but with a different wavefront at each mirror. These two cases correspond to near-flat h^F and near concentric h^C mirror shapes. According to Eqns. 11 and 12, the Mesa beam describes the electric field distribution at a near-flat mirror, whereas the Gaussian beam is referred to the near-concentric mirror. To construct a near-concentric mirror $h^C(\vec{r})$ for the Mesa beam, we used the relation between near-flat and near-concentric cases, as follows:

$$h^F(\vec{r}) + h^C(\vec{r}) = \frac{r^2}{L}. \tag{13}$$

The product r^2/L is the surface height of an ideal concentric mirror with respect to a flat mirror. Mirror shapes for the three cases: concentric Gaussian (CG), concentric Mesa (CM), and flat Mesa (FM) are shown in Fig. 3. If the grid size for the mirror surface area S is sufficiently fine, then the electric field E across element area $\mathrm{d}^2\mathrm{r}$ becomes quasi-steady [46], and Eqn. 7 can be simplified to:

$$E_2(\vec{r_2}, L) = N_{12} E_1(\vec{r_1}, 0), \tag{14}$$

where

$$N_{12} = \frac{ik}{2\pi} \int\int_S K(\vec{r_2}, \vec{r_1})\, d^2\vec{r_1}. \tag{15}$$

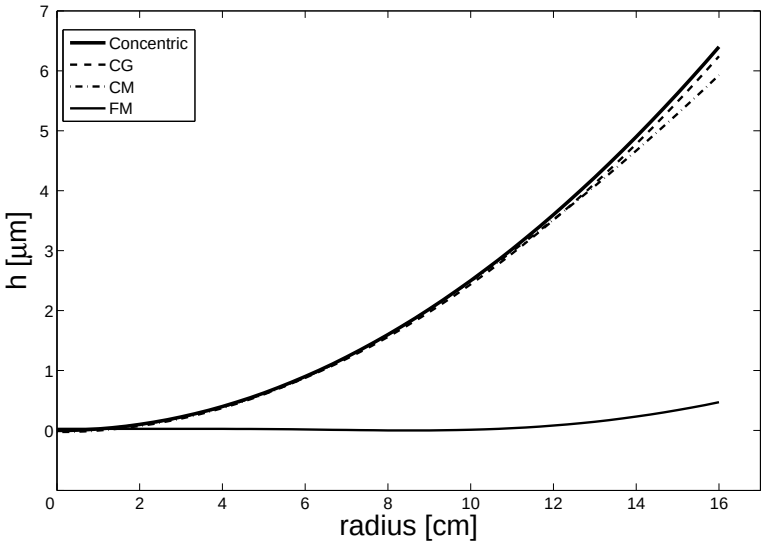

FIG. 3: Mirror shapes for the ideal concentric mirror (solid thick line), concentric Gaussian mirror CG (dashed line), concentric Mesa mirror CM (dash-dotted line), and flat Mesa mirror FM (solid thin line).

Thus, we can introduce an eigenvalue equation, as follows:

$$\gamma E_1 = N_{12} N_{21} E_1, \tag{16}$$

where the complex coefficient γ is the eigenvalue corresponding to the eigenvector E_1, and N_{12} is the kernel integral over the mirror surface for a beam propagating from mirror 1 to mirror 2. The eigevector represents one of the cavity modes which can be sustained at resonance. The amplitude $|\gamma|$ in Eqn. 16 can be interpreted as beam attenuation due to the diffraction losses per round-trip, and is expected to be less than 1. By solving Eqn. 16, we obtain the set of eigenvectors which satisfy the orthogonality relation $\int E_1^i \cdot E_1^{j*} d\vec{r} = \delta_{ij}$ for any i and j eigenvectors. Therefore these eigenvectors can be considered as a basis which spans the space of the cavity states. Each cavity state is defined by one or more eigenvectors (in the case of degeneracy) and its eigenvalue. Eigenvectors contain information about the electric field distribution and the wavefront of the optical mode, whereas eigenvalues carry information about frequency and mode loss. In our case, the basis includes both non-degenerate and 2-fold degenerate eigenvectors. The degeneracy is due to the fact that some eigenvectors occur in pairs, having the same eigenvalues. Such degenerate eigenvectors

correspond to the identical optical mode with different spacial orientation. More about mode orientation is presented in Section IV.

The grid size was determined by checking the convergence of the eigenvalues for a range of grid dimensions. By solving Eqn. 16 with a uniform quadratic grid size of 3.4 × 3.4 mm, we obtained a set of eigenvectors corresponding to mode shapes and eigenvalues, which contain information about phase and diffraction losses. For the purpose of our analysis, we calculated 46 optical modes. We chose only one mode from each degenerate pair which reduced the number of modes down to 25. This allows us to substantially shorten the computational time for the parametric instability analysis. The list of all 25 modes is shown in Table II.

B. High-Order Mode resonances

Resonance frequencies of the high-order modes were estimated using eigenvalues obtained from Eqn. 16. The phase angle between two eigenvalues corresponds to the Gouy phase difference between two modes. Therefore, the HOM frequencies of f_{hom} with respect to the carrier mode frequency f_0 could be calculated according to Eqn. 17:

$$\Delta\nu_{f0} = \frac{FSR}{\pi}\left(arg\left(\gamma_f\right) - arg\left(\gamma_0\right)\right), \tag{17}$$

where $FSR = c/2L$ is the free spectral range. The concentric case for the Mesa beam was estimated using two different approaches. In the first approach, we constructed a nearly concentric mirror and solved Eqn. 16. In the second approach, we used data obtained from the nearly planar Mesa cavity analysis, and used the duality relation $\gamma^C = e^{-i4kL}\left(\gamma^F\right)^*$ to obtain the concentric case [47]. Both results agreed within 0.1 % accuracy. This entire analysis was initially performed for a FM cavity. Fortunately, the good agreement with the duality relation ensured that conversion between the FM and CM solutions could be made analytically. Since we already had data for the FM solution, we used them to obtain the CM cavity parameters. In Fig. 4, we show the first 25 optical modes for the two different cavities. Modes for which $\Delta\nu \geq FSR$, are contracted modulo FSR to appear in the 0-1 FSR range, since they exist as high-order modes of any nearby axial mode. In other words, modes with $\Delta\nu \geq FSR$ are associated with the axial mode $M < 0$. The axial mode index M defines allowed carrier resonant frequencies, and has a value of $M = 0, \pm1, \pm2, \pm...$.

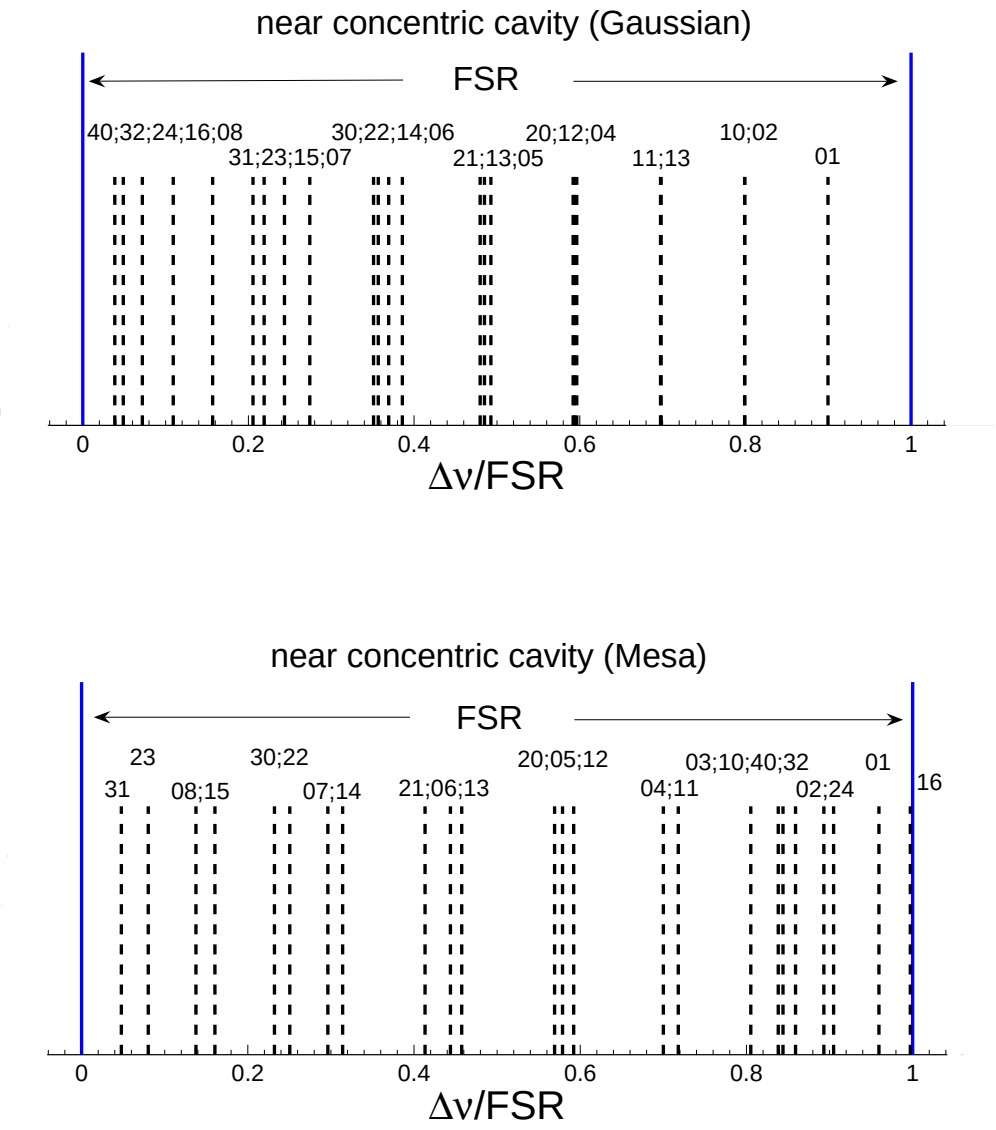

FIG. 4: Near-concentric cavity structures for Gaussian and Mesa cavities. Each dashed vertical line corresponds to a higher-order mode frequency lying in the 1st FSR. The number above each vertical line refers to the mode type listed in Table II.

Due to the duality relation, the CM cavity structure in the 1st FSR range is:

$$\Delta\nu^C = M \cdot FSR - \Delta\nu^F, \text{ with M} = 1, \tag{18}$$

where superscripts C and F correspond to the concentric and flat case, respectively. According to the above equation the HOM location relative to the FSR is swapped between the concentric and the flat cavity. In the flat cavity, the mode location is shifted toward higher values of M with increasing mode order; whereas for concentric cavities, the mode location is shifted

toward lower M with increasing order. Note that both the optical field pattern and the spatial displacement pattern of the mirror reflecting surface have cylindrical symmetry. Moreover, both patterns increase complexity in the same fashion (radial and azimuthal divisions) with increasing mode frequencies. Therefore, the near-concentric cavities have an intrinsic mismatch between lower-order acoustic modes and lower-order optical modes. This is beneficial for the PI situation. As shown in Appendix A, the CM cavity has a unique mode distribution, with increasing Gouy phase such that $arg(\gamma_{i-1}) - arg(\gamma_i) << arg(\gamma_{i+1}) - arg(\gamma_i)$. It seems that the mode spacing in such a cavity becomes significantly larger with an increase of the mode order, in comparison to the Gaussian concentric cavity.
We now go on to estimate the losses for the optical cavity high-order modes.

C. Cavity losses

The optical loss of the cavity high-order modes directly determines the parametric gain R for the opto-acoustic interactions. There are two dominant sources of loss: coupling losses due to the transmissivity of the input mirror, and diffraction losses which are associated with mirror geometry and mode shape. Since parametric gain is proportional to the quality factor of the optical modes, the Q-factor for each optical mode needs to be estimated. The loss parameter δ from Eqn. 1 is defined as follows:

$$\delta_f = -\frac{FSR}{4\pi} ln\left[\left(1-\sigma_f\right)\left(1-T_1\right)\left(1-T_2\right)\right]. \tag{19}$$

Here T_1 and T_2 is the transmissivities of each of the two mirrors, and σ_f is the diffraction loss of the optical mode per round-trip. The eigenvalues are related to the diffraction losses as follows:

$$\sigma_f = 1 - |\gamma_f|^2. \tag{20}$$

According to the duality relation [47], both FM and CM cavities have the same diffraction losses. Therefore, we adopt the σ values of the Flat Mesa cavity for the CM cavity. The diffraction losses are shown in Fig. 5. Appendix A presents Table II relating mode number to the conventional mode shape notation (TEM pq). Note that the fundamental CG and Mesa (either FM or CM) modes (ie. mode #1 in Fig. 5 corresponding to the TEM 00 mode) have the same loss for both types of beams, as determined by our design criteria. The σ-value for HOMs is strongly dependent on the mode shape. Modes with the same order

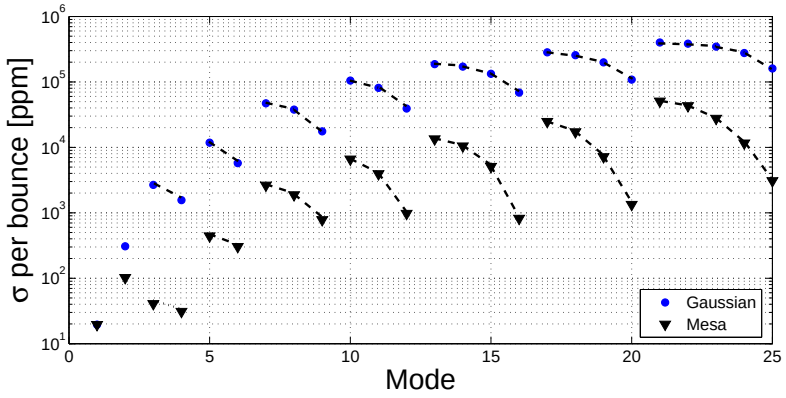

FIG. 5: Diffraction losses for concentric cavities. The x-axis corresponds to the mode number shown in Table II (Appendix A).

have substantially different losses. This effect is more prominent for the Mesa cavity. There is a noticeable difference in the magnitude of the losses between the two types of cavities. The losses of the HOMs for the CG cavity are much higher than for the Mesa cavities. Fig. 5 shows that the losses of all mode families increase with radial mode index q, but decrease with azimuthal mode index p, except for the particular case of the second and third modes, for which these trends are reversed.

Smaller diffraction losses for Mesa beams mean narrower peaks, and higher Q-factors. The quality factor is defined as:

$$Q_f = \frac{-2\pi\nu_f}{FSR \cdot ln\left[\left(1-\sigma_f\right)\left(1-T_1\right)\left(1-T_2\right)\right]}. \tag{21}$$

The Q-factor upper limit is set by coupling losses, and has a value of $\sim 3{\cdot}10^{12}$. Due to the diffraction losses, the Q-factor is reduced below the value set by the transmissivity of the mirrors. Fig. 6 shows the Q-factor as a function of mode number for both cavities. There is a distinguishable difference between CG and CM modes. Most of the Mesa beam cavity modes have a Q $> 10^{12}$. Diffraction losses only significantly reduce the Q-factor for the higher orders of the modes considered. For all modes with radial index p = 0, the diffraction loss has a very small impact on the mode Q-factor. On the other hand, Gaussian HOM diffraction losses cause their Q-factor to be reduced by a factor ~ 10. Only a few of the first low-order modes have a Q-factor set by coupling losses.

Since parametric gain is directly proportional to the optical Q-factor, the higher Q-factor

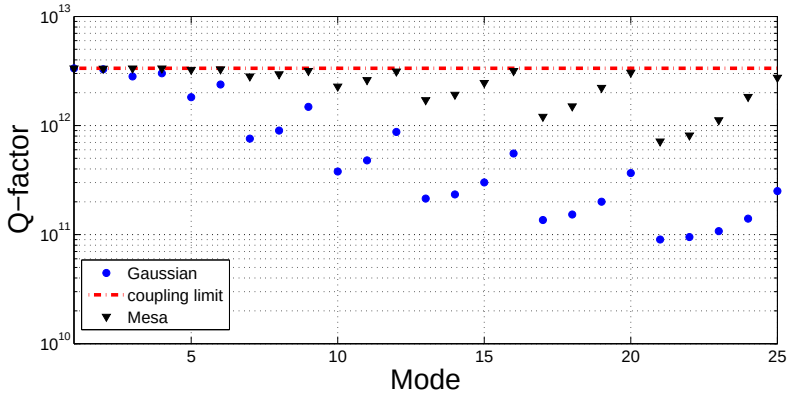

FIG. 6: Q-factor of the optical modes for CM and CG cavities. The dashed line corresponds to the coupling limit of the cavities. The x-axis corresponds to the mode number shown in Table II (Appendix A).

of the Mesa cavity optical modes acts to increase parametric instability as compared to the Gaussian cavity.

We now go on to determine the critical geometrical overlap of the optical modes described in Sec. III with the acoustic modes described in Sec. II.

IV. OPTO-ACOUSTIC INTERACTION: THE MODE OVERLAPPING FACTOR

A low-loss resonant 3-mode interaction (for which $\Delta\omega \approx 0$) is not sufficient to ensure that the parametric gain will exceed unity. The gain also depends on the magnitude of the geometrical overlap between the modes,which is defined by the overlapping parameter Λ. Mathematically, three modes - consisting of the carrier E^{00}, the high-order mode E^{hom}, and the acoustic mode μ - must have a spatial match defined by the integral $\int E^{00}(\vec{r})E^{*hom}(\vec{r})\mu_{\perp}(\vec{r})d\vec{r_{\perp}}$, where $\mu_{\perp}$ is the displacement vector of the acoustic mode normal to the test mass surface. The higher this integral value, the better is the overlap between modes. Moreover, each acoustic mode μ has different strain energy, due to the difference in spatial displacements between modes. In other words, each acoustic mode varies in the fraction of the total mass which vibrates. Such a fractional mass, called the effective mass, refers to the excitation susceptibility of an acoustic mode. If the effective mass is large then

the energy required to induce vibration is also high. A normalised overlapping parameter between the *ith* HOM and *jth* acoustic mode can be written as:

$$\Lambda = \frac{V\left(\int E^{00}\left(\vec{r}\right) E^{*hom}\left(\vec{r}\right) \mu_{\perp}\left(\vec{r}\right) d\vec{r_{\perp}}\right)^{2}}{\int |\mu\left(\vec{r}\right)|^{2} d\vec{r_{\perp}} \int |E^{00}\left(\vec{r}\right)|^{2} d\vec{r_{\perp}} \int |E^{hom}\left(\vec{r}\right)|^{2} d\vec{r_{\perp}}}, \tag{22}$$

where the product $V/\int |\mu\left(\vec{r}\right)|^{2} d\vec{r_{\perp}}$ is the mass ratio of the mass of the test mass to the effective mass of the acoustic mode.

In our analysis, we estimated the maximal overlapping parameter Λ by rotation of the optical mode with respect to the position of acoustic mode. The reason why we performed mode rotation comes from the fact that an optical eigenvector solution gives degenerate modes (modes with the same γ) oriented with respect to each other by $\pi/(2\mathrm{p})$, for the same (p,q) type with $\mathrm{q} \neq 0$. The indices p and q correspond to radial and azimuthal indices, respectively. Such orientation of the degenerate modes is the result of the orthogonality of the eigenvectors in the solution of Eqn. 16. Each non-radially symmetric mode requires exactly two basis eigenvectors to be fully described. This is analogous to a vector in two dimensional space, which can be defined by two basis vectors spanning the space. Each pair of eigenmodes has the same values of σ and $\Delta\nu$. It is clear that $\Lambda(\phi = 0) + \Lambda(\phi = \pi/(2p)) = \Lambda(\phi = \phi_{maximal})$ for a particular mode. Therefore, to reduce the number of optical modes in the parametric instability analysis, we chose one mode from each pair, and found the angle at which Λ has the largest value. The Λ-values were calculated for all 800 acoustic modes, using a set of 25 optical eigenvectors. To ensure that Λ was calculated with high accuracy, we interpolated an acoustic mode $\mu_{\perp}$ onto the finer optical mode grid, and then rotated the optical mode by 1 deg steps. An example of the Λ-value as a function of rotation angle is shown in Fig. 7. In an ideal cylindrically symmetrical situation, optimal modes would be likely to align themselves to the maximal Λ-value. However, in real situations asymmetry is likely to lock the mode orientations to specific values. Thus, this method of choosing the maximal overlap estimates the worst case for PI.

From the plots in Fig. 7, it follows that CM modes have larger overlaps. One of the factors responsible for high Λ-values is the relatively large size of CM modes with respect to CG modes. Note, however, that the overlapping is a product of three modes. Thus the beam size is not the only factor responsible for large Λ. It also depends on the shape match between optical and acoustic modes. For a particular 3-mode combination, the CG cavity can sometimes have larger Λ. This is shown in Fig. 8. Only optical modes with a value of

a) TEM 01

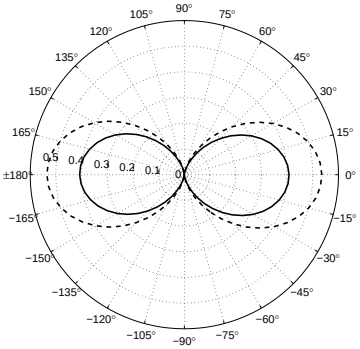

b) TEM 02

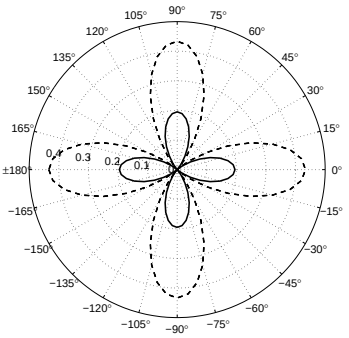

c) TEM 15

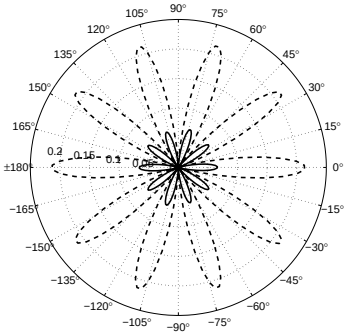

d) TEM 10

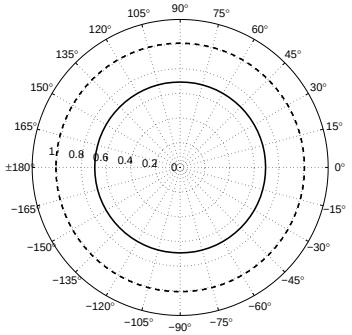

FIG. 7: Overlapping parameters Λ as a function of opto-acoustic mode rotation. The solid/dashed line corresponds to the overlapping of CG/CM modes, respectively. These plots were produced such that Λ^{max} was at $\phi = 0$. Note that for any optical mode of (p,q) type with q = 0, Λ remains constant for an arbitrary ϕ, as expected.

Λ greater than a threshold value Λ_{th} (either Mesa or Gaussian modes) are presented in this figure. The value of Λ_{th} is given by $\Lambda_{th} = \omega_m^2/\vartheta Q_m$, where $\vartheta = \frac{4PQ}{mLc}$. This is the threshold value for Λ overlap for which the opto-acoustic interaction can be potentially dangerous. This quantity was estimated for a constant Q-factor, corresponding to the coupling loss. Fig. 8 shows that the CM cavity has ~ 2 as many cases where $\Lambda > \Lambda_{th}$, as compared to the CG cavity. This indicates that the chance of PI to occure may be higher by a factor of ~ 2 for the Mesa cavity.

By plotting the distribution of the overlaps, we found close similarities in the distribution patterns for both cavities (see Fig. 9). However, they differs in the number of optical modes

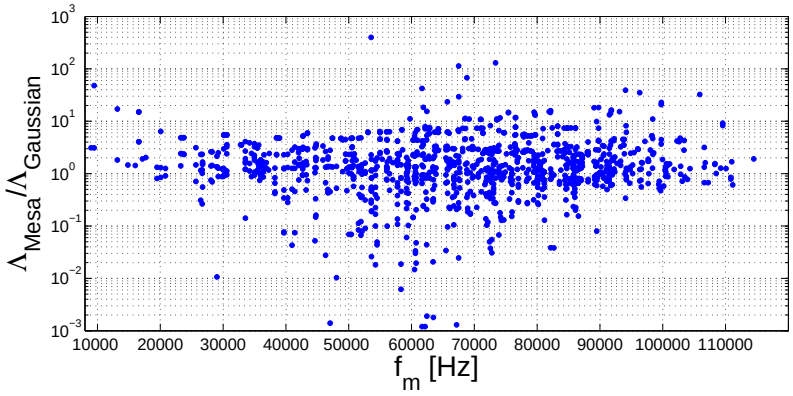

FIG. 8: Ratio of Mesa beam to Gaussian beam overlapping parameters Λ, for a given acoustic mode.

exceeding the Λ-threshold value in various Λ ranges. There are substantially more optical modes in $1 \leq \Lambda < 2$, $2 \leq \Lambda < 4$, and $10 \leq \Lambda < 20$ bins for the Mesa cavity, whereas the other ranges remain almost identical. The diference in each of these bins is $\sim$50% with respect to the Gaussian cavity.

The dependence of Λ on the relative alignment of the optical and acoustic modes shows that designs that lock these modes in particular orientations can be used to minimise the chance of instability from particular modes. However such minimisation of Λ cannot be achieved in general, because of the multiplicity of modes.

The previous sections describe how data was obtained to model parametric instability. We go on to present the results of the PI analysis.

V. PARAMETRIC INSTABILITY

Parametric instability analysis was carried out for a 2-mirror cavity, with parametric gain R estimated according to Eqn. 2. Since we are only interested in determining the relative risk of instability between the two cavity configurations, we assumed the acoustic mode Q-factors to be constant (see Table I), with a $Q_m = 10^7$. This is a typical Q-factor expected with current detector technology. The resonance conditions $\Delta\omega$ for both damping and excitation processes were estimated using 800 acoustic modes. R-values for each mode were calculated by superposition of the excitation and damping processes for all 25 modes.

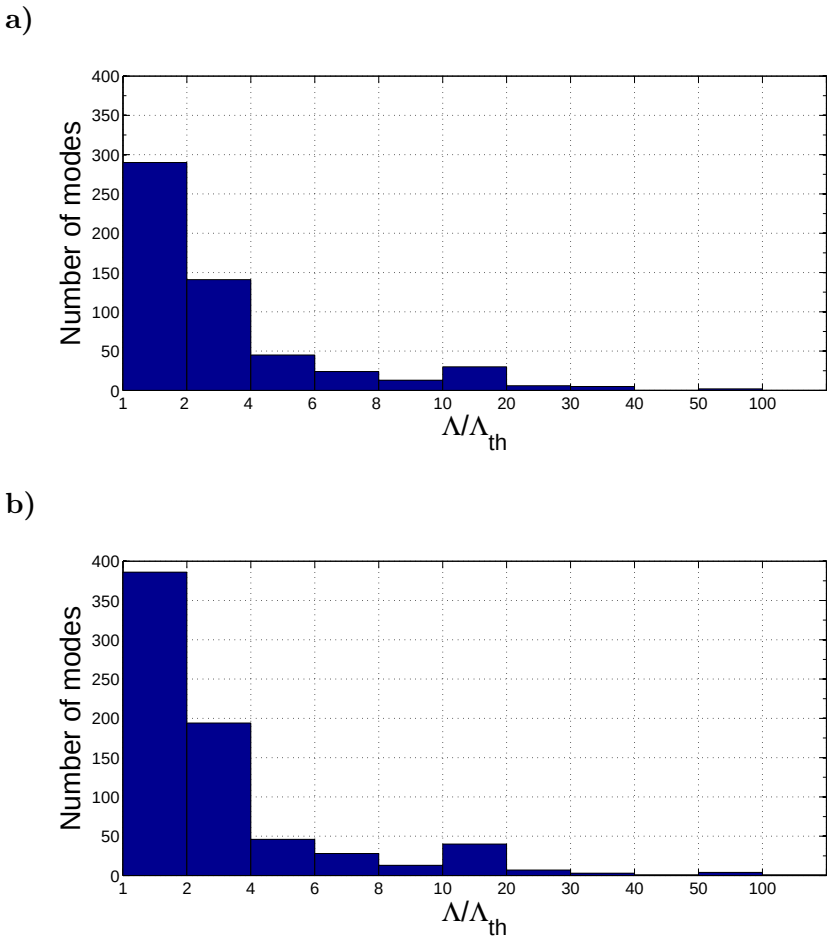

FIG. 9: Histogram of the optical mode distribution in terms of the overlapping parameter Λ. Each bin represents the Λ range normalised by $\Lambda_{th} = \omega_m^2/\vartheta Q_m$, as described in Section IV.

To ensure that all mode interactions with positive and negative gain were taken into account, we extended the $\Delta\omega$ calculation to a range of M = $\pm$ 4 [49]. The parametric gain for 800 modes in the CG and CM cavities is shown in Figs. 10a and 10b, respectively. Each dot represents the R-value for a particular acoustic mode. There are 2 and 10 unstable modes (R $\geq$ 1) for the Gaussian and Mesa cavities, respectively.

As discussed ealier, and explained in Zhao et al. [28], small changes in mirror shape can cause detuning of the optical HOMs, and thus significantly affect parametric instability. For Gaussian cavities, this effect can be explored by considering the dependence of parametric instability on the mirror radius of curvature. We can then allow for manufacturing tolerances and differential thermal distortions of the mirror. Unfortunately, we cannot use the same method for Mesa beams since the cavity is not characterised by a radius of curvature. For

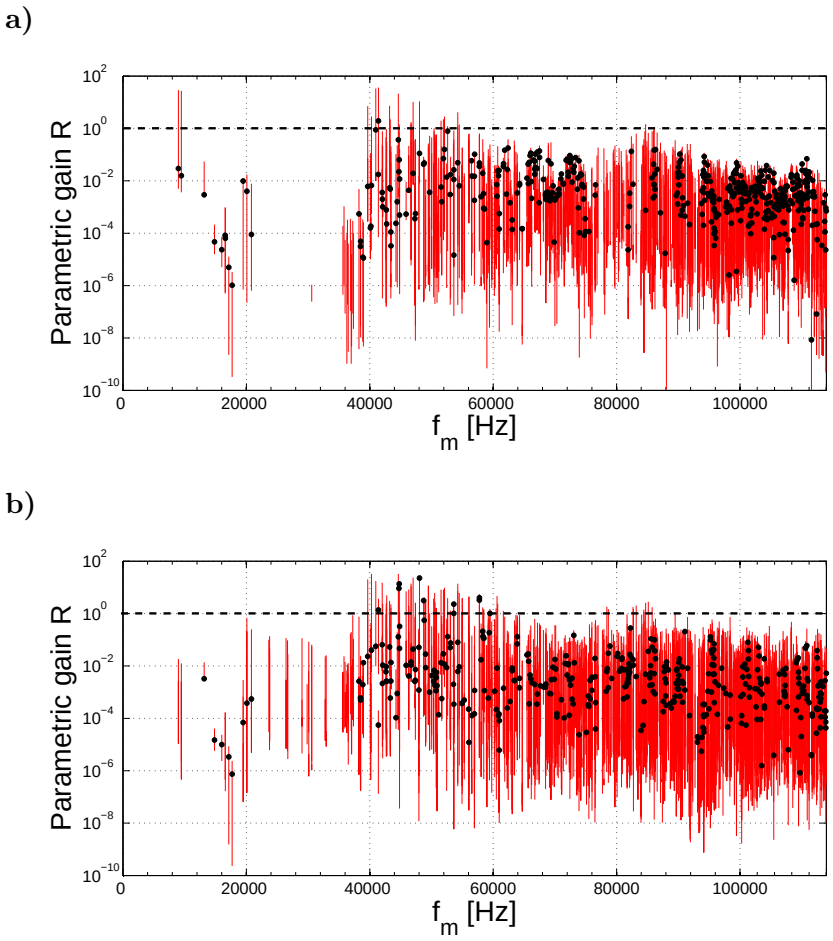

FIG. 10: Parametric gain for concentric (a) Gaussian, and (b) Mesa cavities. Dots represent gains for the resonance condition $\Delta\omega$ estimated from acoustic and optical analysis, whereas the vertical red lines represent gains in the $\Delta\omega$ $\pm 2\pi \cdot 2000$ Hz range.

this reason, we have chosen to consider the gain range for which the resonance condition $\Delta\omega$ is allowed to vary by $\pm$ 2000 Hz. The number of unstable modes will vary dynamically as the thermal condition of the interferometer changes. Such a procedure ensures that all potentially unstable modes are included. The variation of the parametric gain is shown in Fig. 10 as vertical lines. Dots correspond to $\Delta\omega$ values obtained from the optical mode structure and acoustic mode analysis. In Fig. 11, an example is shown of R-value changes for an 85 kHz mode, as a function of $\Delta\omega' = \Delta\omega \pm 2\pi \cdot 2000$ rad/s. Each peak represents an interaction of a different optical mode with the same acoustic mode. In some cases, the resonance peak can be positive with R exceeding unity and causing instability. In some other cases, becomes negative indicating that the acoustic mode will be damped.

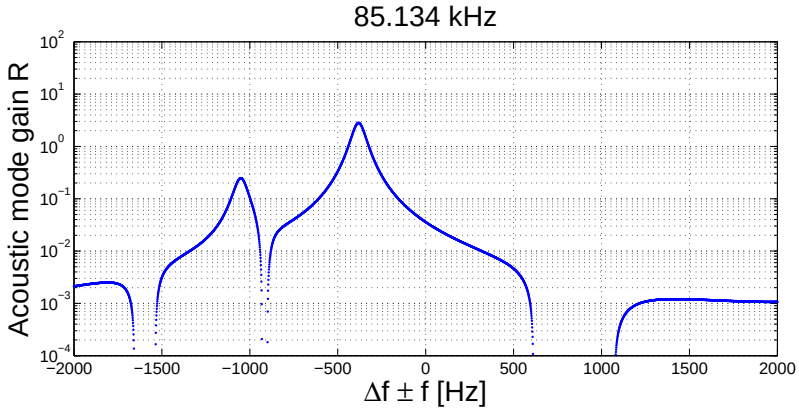

FIG. 11: An example of gain R variation for the 85.134 kHz acoustic mode in the $\Delta\omega/2\pi \pm 2000$ Hz range. Note, variation in R corresponds to the vertical line in Fig. 10.

By counting all modes for which $R \geq 1$ for some values of $\Delta\omega$ in a chosen range, we found that there are as many as 24 and 72 unstable modes per test mass in the CG and CM configuration, respectively. This indicates that the Mesa beam cavity seems to be more susceptible to parametric instability by a factor of ~ 3. The distribution of modes in terms of R-value is shown in Fig. 12. Only modes with $R \geq 0.2$ are presented. In spite of a larger number of unstable modes for the Mesa cavity, the mean gain <R> of the unstable modes is 6.2, whereas for the Gaussian cavity <R> = 8.8.

VI. CONCLUSIONS

Our analysis has revealed several differences between Mesa and Gaussian beam cavities. We found that the overlapping parameter is larger in the Mesa cavity than in the Gaussian cavity, for ∼70% of all acoustic modes. In spite of larger HOM spot sizes, the diffraction losses are smaller than those for the Gaussian cavity by ~ 1 order of magnitude. We were somewhat surprised to find that while the Mesa cavity has a more radially extended field distribution, it simultaneously has low diffraction losses in comparison to Gaussian beams. However, this result is in agreement with mode shape calculations done by Tarallo [48]. These unusual properties of the Mesa cavity modes, i.e. more radially extended electric field but simultaneously lower losses with respect to CG modes, are most probably due to the mirror topography of the Mesa cavity. The rapidly rising edge of both the CM and

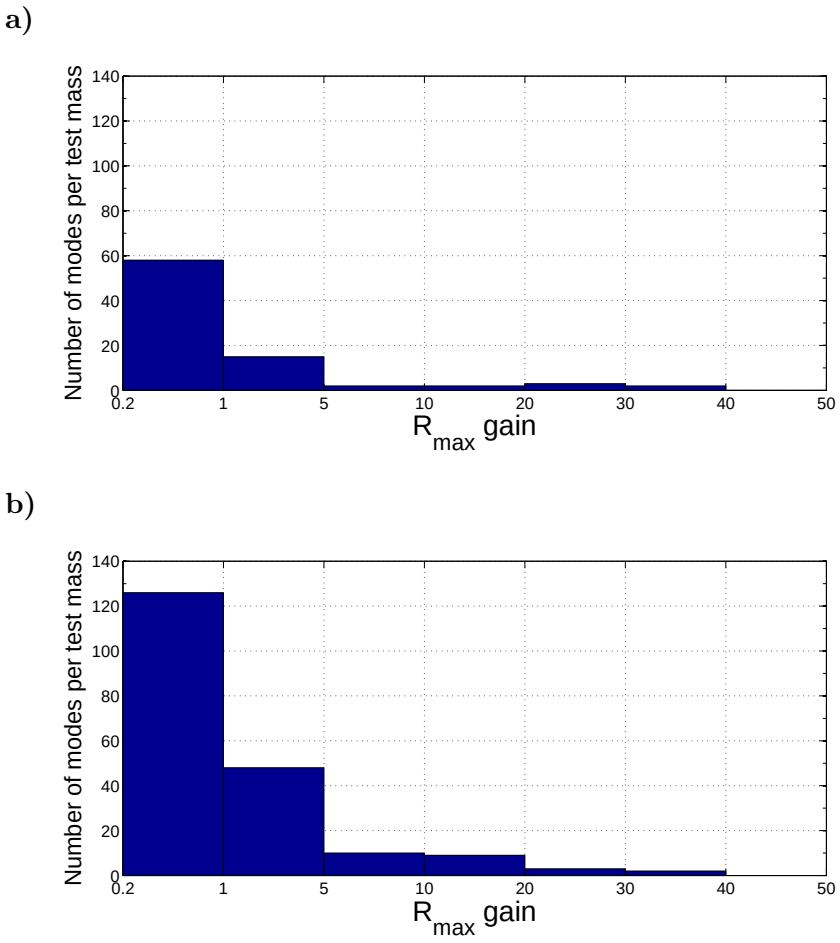

FIG. 12: Histogram of the acoustic modes distribution per test mass in a) the Gaussian cavity, and b) the Mesa cavity, respectively. Only modes with parametric gain R $\geq$ 0.2 are shown.

FM mirrors spreads the HOM field over a relatively larger mirror area, but at the same time confines the light more efficiently than the CG mirror [36]. Because the Mesa beam distributes energy over a larger area of the test mass mirrors than does the Gaussian beam, it is not surprising that the overlapping parameter for the Mesa beam cavity is larger than that of the Gaussian cavity.

The concentric Mesa cavity seems to have a unique mode structure, in which modes are not equally spaced in frequency, whereas the concentric Gaussian cavity modes are more uniformly distributed. The difference in the mode distributions for the CM and CG cavities is quite prominent. This can be seen in the frequency offset data given in Appendix A. For example, modes 3 and 4 (TEM 10 and TEM 02) are almost equal for the CG cavity, but differ by several kHz for the CM cavity. This clearly causes a significant difference in the

parametric instability solutions for the two types of cavity.

The following three factors: the difference in optical structure of the CM cavity, the lower diffraction losses, and the larger overlapping parameters, all have a direct impact on parametric instability. Our analysis shows that for the Mesa beam cavity, there are likely to be $\sim$3 times as many unstable modes as compared with a conventional Gaussian beam interferometer. However, the mean parametric gain is slightly lower. Nevertheless, parametric instability is likely to be a more significant issue for Mesa beams.

Finally, it is important to point out that both the CM and CG cavity systems require a solution to the PI problem. Two methods have been identified - acoustic damping or optical feedback [25]. Our work emphasises that, in both cases, solutions need to be implemented, and given that this can be achieved for CG cavities, it should not be so difficult to extend the solutions to CM interferometers.

Acknowledgments

The authors thank Chunnong Zhao and Pablo Barriga for useful discussion and advice, and Andre Fletcher for help with proofreading this paper. This research was supported by the Australian Research Council and by the Department of Education and Science. This work is part of the Australian Consortium for Interferometric Gravitational Astronomy (ACIGA).

---

[1] C. Wilkinson, LIGO Document: LIGO-G070454-00-M (2007), available at http://www.ligo.caltech.edu/docs/G/G070454-00.pdf.

[2] F. Acernese, et al., J. Opt. A: Pure Appl. Opt. **10**, 064009 (2008).

[3] K. Kuroda and the LCGT Collaboration, Class. Quantum Grav. **23**, 215 (2006).

[4] S. Rowan, R. L. Byer, M. M. Fejer, R. Route, G. Cagnoli, D. R. M. Crooks, J. Hough, P. H. Sneddon, and W. Winkler, Proc. of SPIE **4856** (2003).

[5] T. Uchiyama, T. Tomaru, M. E. Tobar, D. Tatsumi, S. Miyoki, M. Ohashi, K. Kuroda, T. Suzuki, N. Sato, T. Haruyama, et al., Phys. Lett. A **261**, 5 (1999).

[6] K. Yamamoto, S. Miyoki, T. Uchiyama, H. Ishitsuka, M. Ohashi, K. Kuroda, T. Tomaru,

N. Sato, T. Suzuki, T. Haruyama, et al., Phys. Rev. D **74**, 022002 (2006).

[7] M. Bondarescu and K. Thorne, Phys. Rev. D **74**, 082003 (2006).

[8] A. P. Lundgren, R. Bondarescu, D. Tsang, and M. Bondarescu, Phys. Rev. D **77**, 042003 (2008).

[9] V. Braginsky, S. Strigin, S. Vyatchanin, E. D'Ambrosio, R. O'Shaugnessy, and K. Thorne, LIGO Document: LIGO-G010333-00-D (2001), available at www.ligo.caltech.edu/docs/G/G010333-00/G010333-00.ppt.

[10] E. D'Ambrosio, R. O'Shaugnessy, K. Thorne, P. Willems, S. Strigin, and S. Vyatchanin, Class. Quantum Grav. **21**, 867 (2004).

[11] B. Mours, E. Tournefier, and J. Y. Vinet, Class. Quantum Gravity **23**, 5777 (2006).

[12] M. Barsuglia, AstroParticule et Cosmologie Paris (2008), available at wwwcascina.virgo.infn.it/advirgo/biweekly/2008/2008-07/barsuglia_010708.ppt.

[13] M. Bondarescu, O. Kogan, and Y. Chen, Phys. Rev. D **78**, 082002 (2008).

[14] M. G. Tarallo, J. Miller, J. Agresti, E. D'Ambrosio, R. DeSalvo, D. Forest, B. Lagrange, J. M. Mackowsky, C. Michel, J. L. Montorio, et al., Applied Optics **46**, 6648 (2007).

[15] J. Agresti, R. DeSalvo, P. Ganau, J. M. Mackowsky, J. L. Montorio, L. Pinard, B. Simoni, P. Willems, E. D'Ambrosio, D. Forest, et al., LIGO Document: LIGO-G050310-00-R (2005).

[16] J. Miller, Workshop on Optical Coatings in Precision Measurements (2008), available at http://www.ge.infn.it/~gemme/virgo/CoatingWorkshop/miller.pdf.

[17] H. J. Eichler, R. Menzel, and D. Schumann, Appl. Opt. **31**, 5038 (1992).

[18] I. Y. Anikeev and J. Munch, Optics Communications **178**, 449 (2000).

[19] F. V. Kowalski, J. Buhl, and B. McMahon, Applied Optics **41**, 1098 (2002).

[20] O. Arcizet, P.-F. Cohadon, T. Briant, M. Pinard, and A. Heidmann, Nature **444**, 71 (2006).

[21] T. Corbitt, D. Ottaway, E. Innerhofer, J. Pelc, and N. Mavalvala, Phys. Rev. A **74**, 021802(R) (2006).

[22] I. A. Bilenko, E. N. Ivanov, M. E. Tobar, and D. G. Blair, Physics Letters A **211**, 139 (1999).

[23] C. Zhao, L. Ju, Y. Fan, S. Gras, B. Slagmolen, H. Miao, P. Barriga, and D. Blair, Phys. Rev. A **78**, 023807 (2008).

[24] H. Rokhsari, T. J. Kippenberg, T. Carmon, and K. J. Vahala, IEEE Journal of Selected Topics in Quantum Electronics **12**, 96 (2006).

[25] L. Ju, D. G. Blair, C. Zhao, S. Gras, Z. Zhang, P. Barriga, H. Miao, Y. Fan, and L. Merrill,

Class. Quantum Grav. **26**, 015002 (2008).

[26] V. B. Braginsky, S. E. Strigin, and S. P. Vyatchanin, Phys. Lett. A **287**, 331 (2001).

[27] W. Kells and E. D'Ambrosio, Physics Letters A **299**, 326 (2002).

[28] C. Zhao, L. Ju, J. Degallaix, S. Gras, and D. Blair, Phys. Rev. Lett. **94**, 121102 (2005).

[29] H. S. Bantilan and W. Kells, LIGO Document: LIGO-T060207-00-Z (2006), available at http://www.ligo.caltech.edu/docs/T/T060207-00/T060207-00.pdf.

[30] V. B. Braginsky, S. E. Strigin, and S. P. Vyatchanin, Phys. Lett. A **305**, 111 (2002).

[31] S. P. Vyatchanin and S. E. Strigin, Quantum Electronics **37**, 1097 (2007).

[32] S. E. Strigin and S. P. Vyatchanin, Phys. Lett. A **365**, 10 (2007).

[33] W. Kells, LIGO Document LIGO-T060159-00-D (2006), available at http://www.ligo.caltech.edu/docs/T/T060159-00/T060159-00.pdf.

[34] G. Mueller, LIGO Document LIGO-G070441-00-R (2007), available at http://www.ligo.caltech.edu/docs/G/G070441-00/G070441-00.pdf.

[35] L. Ju, S. Gras, C. Zhao, J. Degallaix, and D. G. Blair, Phys. Lett. A **354**, 360 (2006).

[36] P. Savov, K. Thorne, and S. Vyatchanin, LIGO Document: LIGO-G050441-00-Z (2005), available at http://www.ligo.caltech.edu/docs/G/G050441-00/G050441-00.pdf.

[37] W. Kells, LIGO Document LIGO-T060296-00-D (2006), available at http://www.ligo.caltech.edu/docs/T/T060296-00/T060296-00.pdf.

[38] L. Ju, C. Zhao, S. Gras, J. Degallaix, D. G. Blair, J. Munch, and D. H. Reitze, Phys. Lett. A **355**, 419 (2006).

[39] P. Savov and S. Vyatchanin, Phys. Rev. D **74**, 082002 (2006).

[40] H. Grimmer, Acta Cryst. **A62**, 168 (2006).

[41] http://www.ansys.com.

[42] J. K. Cullum and R. A. Willoughby, *Lanczos Algorithms for Large Symmetric Eigenvalue Computations: Theory* (SIAM, 2002), ISBN 9780898715231, p 210.

[43] P. Barriga, B. Bhawal, L. Ju, and D. G. Blair, Journal of the Optical Society of America A **24**, 1731 (2006).

[44] R. O'Shaughnessy, S. Strigin, and S. Vyatchanin (2004), arXiv:gr-gc/0409050v1.

[45] P. A. Belanger and C. Pare, Optics Letters **16**, 1057 (1991).

[46] C. Yuanying, W. Youqing, H. Jin, and L. Jiarong, Opt. Comm. **23**, 1 (2004).

[47] J. Agresti, Y. Chen, E. D'Ambrosio, and P. Savov (2005), arXiv:gr-gc/0511062.

[48] M. G. Tarallo, Ph.D. disseration, LIGO Document: LIGO-P050032-00- (2005), available at http://www.ligo.caltech.edu/docs/P/P050032-00.pdf.

[49] The range is extended to M = ± 4 in order to cover acoustic modes which exceed the 3rd FSR in Fig. 2

APPENDIX A: OPTICAL SPECTRUM OF THE CG VS. CM CAVITIES

TABLE II: Optical mode structure for CG and CM cavities. Column 2 is the list of optical mode types used in the analysis. Indices p and q correspond to the radial and azimuthal numbers of the mode. Columns 3 and 5 show the difference between the carrier frequency at M = 0 and the higher order mode. Note that all HOMs are intentionally shown in the 1st FSR range. Columns 4 and 6 give the diffraction losses per bounce for each of the beams.

		Gaussian cavity		Mesa cavity	
No.	Optical mode (p,q)	$\Delta\nu$ [Hz] modulo FSR	σ [ppm] (per bounce)	$\Delta\nu$ [Hz] modulo FSR	σ [ppm] (per bounce)
1	Carrier	0	19.5	0	19.5
2	01	33710.5	307.9	35957.1	101.9
3	10	29942.9	2664.3	31415.2	40.7
4	02	29945.3	1560.9	33474.3	31.0
5	11	26137.2	11804.1	26907.3	441.3
6	03	26164.3	5742.7	30180.2	303.0
7	20	22184.2	47090.3	21330.8	2633.1
8	12	22239.4	37693.6	22193.5	1876.4
9	04	22346.1	17555.6	26237.8	782.0
10	21	17975.4	104682.0	15487.9	6580.1
11	13	18174.1	81114.0	17143.0	3934.5
12	05	18463.7	39173.2	21690.9	974.5
13	30	13152.7	186679.6	8699.0	13405.0
14	22	13367.4	171579.3	9389.8	10448.0
15	14	13840.4	133066.3	11774.1	5084.5
16	06	14461.1	68653.9	16630.8	820.3
17	31	7700.8	283251.4	1792.1	24745.5
18	23	8207.6	255613.5	3007.7	17209.1
19	15	9125.2	199114.1	6012.7	7148.0
20	07	10270.0	108363.7	11107.5	1336.3
21	40	1449.6	399645.5	31627.7	50575.6
22	32	1832.1	383499.9	32198.3	43076.4
23	24	2694.7	346229.6	33910.0	27662.0
24	16	4095.3	276326.1	37368.5	11592.5
25	08	5878.3	160220.1	5157.1	3078.3